Journal of Oceanography
https://doi.org/10.1007/s10872-023-00702-8

ORIGINAL ARTICLE

Seasonal variation in the current field and development of bottom cold water in Harima-Nada

Siraporn Tong-u-dom[1] · Akihiko Morimoto[2] · Qian Leng[1] · Xinyu Guo[2]

Received: 16 February 2023 / Revised: 6 July 2023 / Accepted: 17 August 2023

Abstract
We investigated the seasonal variation in the current field in Harima-Nada using a high-resolution three-dimensional numerical model. The model showed sufficiently good performance at recreating its spatial and seasonal variation. Additionally, the model successfully reproduced the observed temperature and salinity patterns and values, as well as the observed surface current fields. The seasonal variation was consistent with previous studies, showing downwind circulation in winter induced by northwesterly winds and cyclonic circulation in summer induced by density-driven circulation. The water was well-mixed during winter and stratified in summer. During summer, a bottom cold water (BCW) dome develops beneath the thermocline in the central basin, where a surface cyclonic eddy occurs. Cold water from the previous winter is trapped at the bottom in topographic depressions after the onset of spring, forming BCW in the Harima-Nada (HNBCW). Meanwhile, pressure gradients associated with the density difference across the BCW drive geostrophic flow and form a cyclonic eddy at the surface above the HNBCW. HNBCW experiences a temperature increase of approximately 12.8 °C from spring to summer, which is associated with vertical diffusion and horizontal advection processes. Air–sea heat flux is the main factor influencing water temperature and its changes in the HNBCW. In addition, topographic features and river discharge factors affected water circulations as well as the formation and variation in the HNBCW. Harima-Nada is a small, shallow semi-enclosed coastal sea, and therefore any small change in these dynamic factors can affect water characteristics.

Keywords Hydrodynamic model · Seasonal variation · Bottom cold water · Cyclonic eddy · Harima-Nada · Seto Inland Sea

1 Introduction

Harima-Nada is a basin of the Seto Inland Sea (SIS) that is connected to Hiuchi-Nada, Osaka Bay, and Kii Channel through narrow straits named the Bisan, Akashi, and Naruto Straits, respectively (Fig. 1). Harima-Nada is surrounded by Honshu and Shikoku Islands, which are intensively urbanized and industrialized. Its area and average water depth are 3400 km^{-2} and 26 m, respectively (Yanagi 2008), and the basin contains numerous islands in its northern and western parts. These complex geographic features are essential to the physical processes and biogeochemical activities of the basin. Several rivers supply freshwater and nutrients to Harima-Nada, supporting an abundant system that is a major fishing ground and aquaculture site for fish, oysters, and seaweed (Nishikawa et al. 2011). With the increase in human activities associated with rapid economic growth in the 1960s–1970s, Harima-Nada became one of the areas of the SIS that was most seriously impacted by eutrophication (Yamamoto 2003). To alleviate this problem, the Interim Measures Law for Conservation of the Environment of the SIS (later designated the Special Measures Law) was enacted to control and limit total allowable pollutant loads to the environment from industrial and urban sources. As a result, phosphorus and nitrogen loads into the SIS were reduced by 55% and 45%, respectively, between 1979 and 2009 (Boesch 2019), and some areas of the SIS gradually became oligotrophic coastal systems. In recent years, oligotrophication has become a problem, driven by nutrient depletion. The change in nutrient concentrations is associated with decreases in fisheries production affecting small pelagic fish, shellfish, and cultivated nori (*Pyropia*) (Abo and Yamamoto 2019).

✉ Siraporn Tong-u-dom
aommy_se7en@hotmail.com

[1] Graduate School of Science and Engineering, Ehime University, Matsuyama, Japan

[2] Center for Marine Environmental Studies (CMES), Ehime University, Matsuyama, Japan

Published online: 30 August 2023

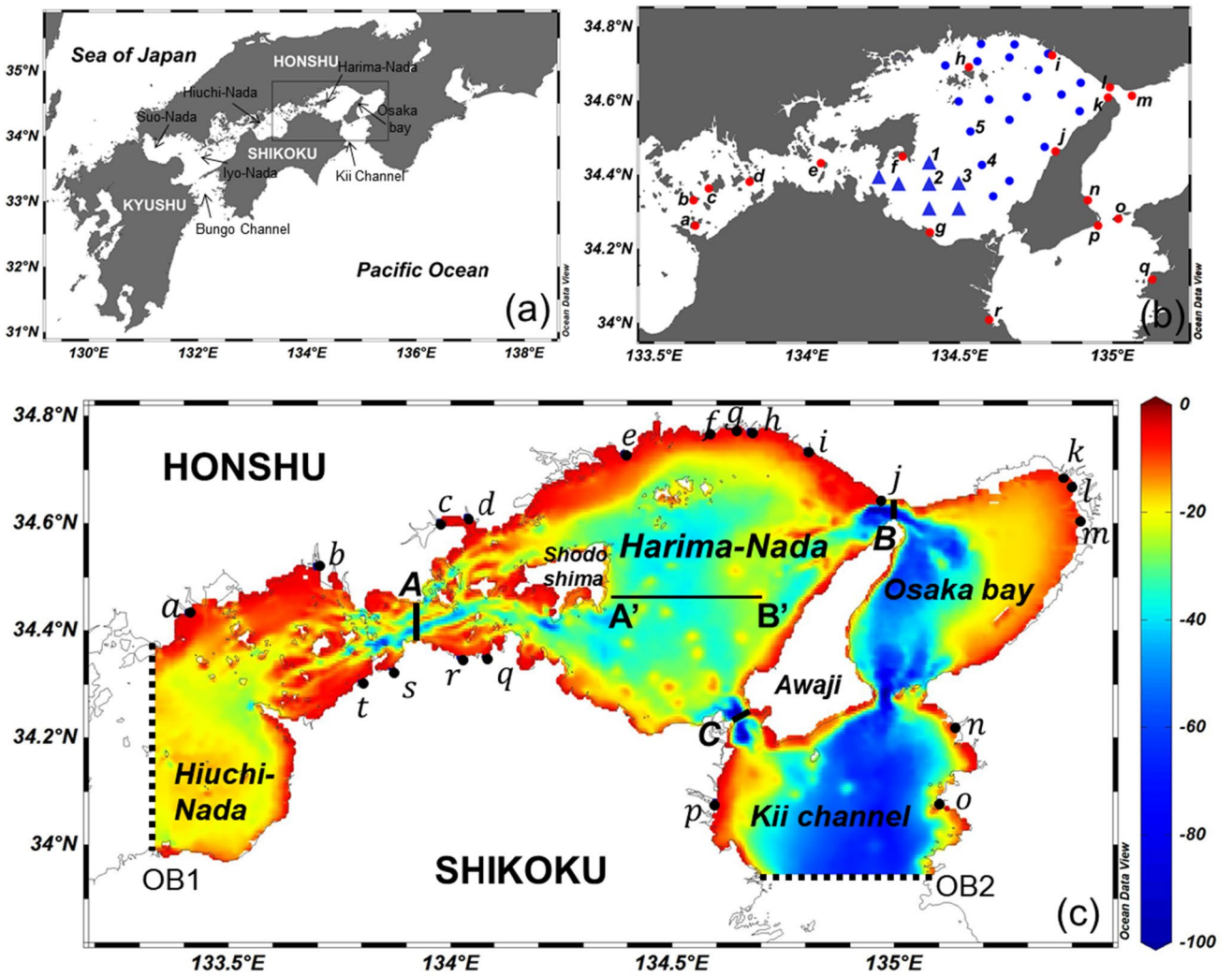

Fig. 1 The locations of the SIS and the Harima-Nada (**a**). Locations of tide gauge and monthly observation stations (**b**). Bathymetry (unit: meters) and model domain for the Harima-Nada (**c**). In **b**, the red dots with lowercase letters (a–r) represent the tide gauge, while the blue dots and triangles denote the monthly observation stations. The number 1 to 5 denote the selected stations used to validate the model results for the vertical profile of temperature in Fig. 6. In **c**, the dotted lines in Hiuchi-Nada (OB1) and Kii channel (OB2) represent the open boundaries of the hydrodynamic model. The black solid circles with lowercase letters (a–t) in **c** are the locations of the rivers. The bold solid lines with upper case letters (A–C) represent the narrow straits that are connected to other bays (e.g., A: Bisan Strait, B: Akashi Strait, and C: Naruto Strait). Line A′B′ denotes the section along with hydrographic fields presented in Figs. 9, 13, 14, and 15g–i (color figure online)

Numerical model studies in the SIS have been conducted by many researchers (e.g., Kobayashi et al. 2006; Chang et al. 2009; Yu et al. 2016; Yu and Guo 2018; Wang et al. 2019; Zhu et al. 2019). These studies have reported that the circulation pattern in the SIS shows strong seasonal variation and differs among basins due to the complex geography of this region. Kobayashi et al. (2006) suggested that tidal currents and tidal energy dissipation are strong in and around the straits, and relatively weak in basins, particularly Harima-Nada. Chang et al. (2009) investigated the seasonal variation in circulation throughout the SIS using a three-dimensional model and revealed that northwesterly winds play an important role in the overall circulation of the SIS during the winter season, driving surface downwind and near-bottom upwind circulation patterns. By contrast, density-driven circulation is dominant in summer due to weak winds and strong stratification, generating cyclonic eddies in several basins including Iyo-Nada, Suo-Nada, and Harima-Nada. Such cyclonic eddies are associated with surface warm pool and bottom cold dome structures (Guo et al. 2004; Chang et al. 2009; Yu et al. 2016; Yu and Guo 2018; Zhu et al. 2022). However, no previous studies have focused on Harima-Nada.

Bottom cold water (BCW), also known as a bottom cold dome, generally forms in spring, is well-developed in summer, and disappears in autumn. It has lower temperatures than surrounding waters and has been widely observed in several shelf seas, including the Irish Sea (Horsburgh and Hill 2003; Holt and Proctor 2003), Yellow Sea (Xia et al. 2006; Yuan et al. 2013; Zhu et al. 2018), Korean Strait (Cho and Kim 1998; Johnson and Teague 2002; Kim et al. 2006), and Bungo Channel (Takeoka et al. 2000; Kaneda et al. 2002). Moreover, this phenomenon has been reported in small-scale areas such as the SIS (Guo et al. 2004; Kobayashi et al. 2006; Kasai et al. 2007; Yu et al. 2016; Yu and Guo 2018; Zhu et al. 2022). The formation of BCW depends on geographic features, and has two main formation mechanisms: cold water from the previous winter is trapped in topographic depressions after the onset of the spring season (e.g., cold water masses in the Irish Sea, Yellow Sea, and SIS), which is the most commonly described process, and cold water mass intrusion from adjacent seas (e.g., Bungo Channel bottom layer intrusion and Korean Strait BCW). The presence of BCW in Harima-Nada (hereafter, HNBCW) has been demonstrated through hydrographic observation (Kobayashi et al. 2006) and recreated in a three-dimensional numerical ocean models (Chang et al. 2009; Yu and Guo 2018).

The BCW and associated cyclonic eddy play important roles in heat transport, water exchange, and biogeochemical activities. For example, a cyclonic eddy in the eastern part of Hiuchi-Nada, which is located on the western side of Harima-Nada, prevents water exchange between the center and outer edges of the eddy; in addition, a bottom cold dome is present, with oxygen-deficient waters formed in the central part of the eddy (Ochi and Takeoka 1986; Takeoka et al. 1986; Guo et al. 2004; Kasai et al. 2007). Furthermore, Abe et al. (2015) suggested that nutrient concentrations and apparent oxygen utilization increase in summer in association with the formation of BCW in Suo-Nada. Yoshie et al. (2011) suggested that breakdown of the BCW in autumn likely supplies nutrients to the surface layer, supporting the autumn diatom bloom in Iyo-Nada. As noted above, BCW is associated with a cyclonic eddy that influences coastal environments and ecosystems throughout the wide basin, and thus may influence fluctuations of nutrients and the ecosystem of Harima-Nada.

As BCW plays significant roles in heat transport, water exchange, nutrient cycling, and biogeochemical processes, clarification of the mechanisms, controlling factors, and intensification of the HNBCW would be useful. Therefore, we focused on spatial and temporal variation in circulation and the development of BCW using a high-resolution, three-dimensional numerical model and examined the generation mechanism and driving factors of BCW and cyclonic eddy formation in Harima-Nada.

2 Model description

2.1 Hydrodynamic model and data input

The hydrodynamic model used is based on the Princeton Ocean Model (POM) (Blumberg and Mellor 1987), a three-dimensional, sigma-coordinate model with a primitive equation. The momentum turbulent closure scheme (Mellor and Yamada 1982) and Smagorinsky formulation (Smagorinsky 1963) are used to calculate vertical and horizontal turbulence mixing, respectively. The model domain covers the eastern part of Hiuchi-Nada, Harima-Nada, Osaka Bay, and part of the Kii Channel from 133.34° E to 135.48° E and 33.95° N to 34.82° N (Fig. 1c). The bottom topography for the model was obtained from a nautical chart with 250 m resolution. The model resolution was set to approximately 500 m in the horizontal directions (1/220 degree in the meridional direction and 1/180 degree in the zonal direction) and 11 vertical sigma levels. The domain has two open boundaries, namely, the western boundary in Hiuchi-Nada (OB1) and the southern boundary at Kii channel (OB2). To characterize the typical seasonal variation in circulation and BCW formation, climatological data were used in the hydrodynamic model. The model was continually repeated for 3 years to achieve a stationary state and the results were saved at an hourly interval during the last year.

Daily atmospheric data (e.g., wind stress and air–sea heat flux) were considered a major forcing factor in the simulation of the hydrodynamic model, detailed descriptions of which were provided by Chang et al. (2009). Daily river discharge data from multiple years (2000–2019) obtained from the Ministry of Land, Infrastructure, Transport, and Tourism were also used in this calculation. The model includes 11 major rivers and 9 secondary rivers, the locations of which are shown in Fig. 1c. The monthly salinity, water temperature, and velocities obtained from prognostic modeling across the whole SIS (Chang et al. 2009), as well as the amplitude and phase of the tide and tidal currents based on the M_2, S_2, O_1, and K_1 constituents obtained from the two-dimensional Harima-Nada model were applied as boundary conditions at the two open boundaries.

The Harima-Nada was characterized by four seasons: spring (March–May), summer (June–August), autumn (September–November), and winter (December–February). The monthly variation in wind stress, air–sea heat flux, and river discharge are presented in Fig. 2. During the spring season, wind stress is relatively weak, and no dominant direction is apparent. In the summer and autumn seasons, the stress remains weak, but southeasterly and northeasterly winds are dominant. In winter, strong

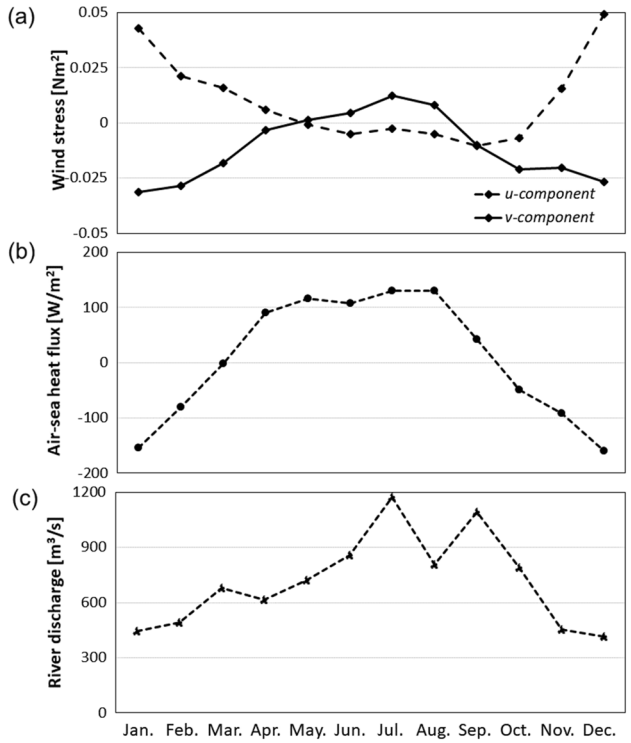

Fig. 2 Monthly averaged climatological mean of **a** wind stress, **b** air–sea heat flux, and **c** river discharge used in the calculation of the hydrodynamic model in Harima-Nada. The positive u- and v-component of wind stress in **a** are eastward and northward, respectively. Positive heat flux in **b** indicates that the ocean gains heat

northwesterly wind stress is dominant. The net air–sea heat flux is negative in winter and late autumn, which means that the sea surface loses heat and water temperature decreases. By contrast, net air–sea heat flux is positive, which means that the sea surface gains heat and water temperatures increases during the spring and summer seasons. In general, river discharge is low throughout the year except during summer. Total river discharge reaches its maximum (2242 $m^3\ s^{-1}$) in July and minimum (363 $m^3\ s^{-1}$) in December, with a mean value of 716 $m^3\ s^{-1}$.

2.2 Observation data

Tidal harmonic constants along the coastline calculated by the Hydrographic and Oceanographic Department, Japan Coast Guard (https://jdoss1.jodc.go.jp/vpage/tide.html) were used to validate model results, as were monthly water temperature and salinity. Data from 19 stations were observed by Hyogo Prefectural Fisheries Department over 20 years (2000–2020), and those from 7 stations were observed by Kagawa Prefectural Fisheries Department over 9 years (2011–2019). The latter data were collected at a standard depth interval of 5 m and of 0.1 m for Hyogo and Kagawa Prefectural Fisheries Department, respectively. January and July are used as representative months for winter and summer, respectively. The locations of observation points are shown in Fig. 1b, in which blue dots and triangles represent the observation points of Hyogo and Kagawa Prefecture, respectively. In addition, mooring observation data of currents obtained from the Japan Oceanographic Data Center (https://jdoss1.jodc.go.jp/vpage/moor.html) were used for comparison with the modeled currents.

3 Results and discussion

3.1 Validation of the model

To assess model performance, the model results were validated against observational data. First, we compared the amplitude and phase of tidal constituents with observations. Then we compared the spatial distributions of simulated temperature and salinity with monthly observations collected around Harima-Nada. High-resolution data in vertical along stations 1–5 in Fig. 1b were utilized for comparing the vertical profiles of temperature. Finally, we presented the results of observed current fields in the Harima-Nada.

3.1.1 Tidal constituent components

The dominant tidal constituents in Harima-Nada are M_2, S_2, K_1, and O_1, among which M_2 is dominant (Yanagi and Higuchi 1981). We compared these four modeled tidal constituents with observations from 18 tide gauges. Figure 3 shows the tidal amplitude and phase lag calculated from model results and observations (see Fig. 1b for the location of the tide gauges). The comparisons of amplitude and phase lag showed satisfactory agreement for the four tidal constituents between the model and observations. Although the model simulated the observed amplitude and phase lag quite well, weak comparability was found at a few sites for the M_2 and S_2 tidal constituents (Fig. 3a, b). The modeled amplitudes of M_2 around the Akashi Strait were larger than observations, while the simulated phase lags of M_2 and S_2 in Harima-Nada were faster than the observed. These sites are located in areas of complex topography, such as around narrow straits and between islands, that the model could not realistically represent. Nevertheless, comparison of area-averaged values across the model domain for the four tidal constituents included in the model with observations revealed good prediction results for all four tidal constituents in terms of both amplitude and phase lag (Table 1). The coefficients of determination (R^2) for the four tidal constituents in terms of amplitude and phase lag between observations and model results were 0.96 and 0.95, respectively. In addition, the root mean square error (RMSE) was less than 10 cm and 20° for amplitude and phase lag, respectively.

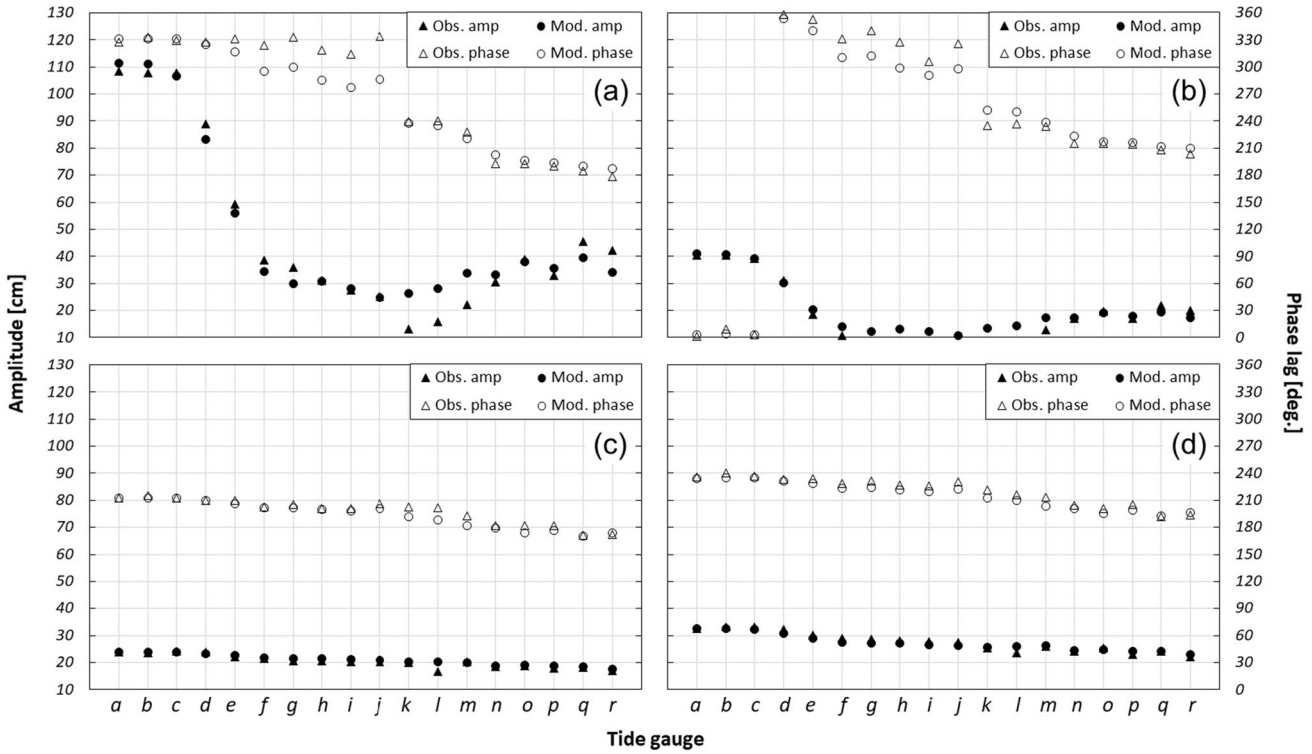

Fig. 3 Comparison of tidal amplitude (left axis) and phase lag (right axis) between observation (triangles) and model simulation (dots). Location of tide gauges is shown in Fig. 1b. The comparison of tidal constituent of M2 tide (**a**), S2 tide (**b**), K1 tide (**c**), and O1 tide (**d**)

Table 1 Comparison of harmonic constants of four tidal constituents between observation and model results

Tidal constituent	Amplitude (cm)				Phase lag (deg.)			
	Obs.	Mod.	R^2	RMSE	Obs.	Mod.	R^2	RMSE
M_2	48.41	49.14	0.96	6.14	273.37	263.44	0.93	17.43
S_2	18.52	20.54	0.95	3.09	228.77	224.12	0.99	13.95
O_1	20.44	20.97	0.97	0.82	197.86	194.06	0.93	4.16
K_1	27.59	27.24	0.95	1.06	220.62	215.78	0.95	3.30

Amplitude and phase lag are area-averaged ones over the model domain

3.1.2 Temperature and salinity

Figures 4 and 5 show the spatial distributions of observed and simulated water temperature and salinity at the near-surface and near-bottom layers in January (winter) and July (summer). During winter, the simulated temperature accurately represents the observed temperature pattern in both surface and bottom layers, showing lower values along the coastline compared to the interior of the basin, although the simulated temperatures are approximately 1 °C higher than observed temperatures. On the other hand, the simulation results represent the observed salinity well in both distribution and value, at approximately 32 throughout Harima-Nada, except around river mouths, where it falls to around 31.0–31.5 in both surface and bottom layers. In summer, the simulation results successfully reproduce the observed temperature and salinity patterns in both surface and bottom layers, although the values were lower than observations by about 1 °C and 0.5, respectively. Both the observed and modeled results indicate the presence of isolated cold water at the near-bottom layer in the central part of Harima-Nada (Fig. 5c, d). Although the BCW in the model is situated in the central basin of the Harima-Nada and extends to deep basin as indicated by 19 °C isotherm, the observed BCW is located slightly northward and spreads in a northeast–southwest direction. These discrepancies of intensity and position of the BCW between model and observation might be due to differences of resolutions; coarse resolution of observed data and high-resolution of model.

We select specific stations corresponding to the BCW region indicated by the 19 °C isotherm to validate vertical structure of the BCW in the model. The comparison

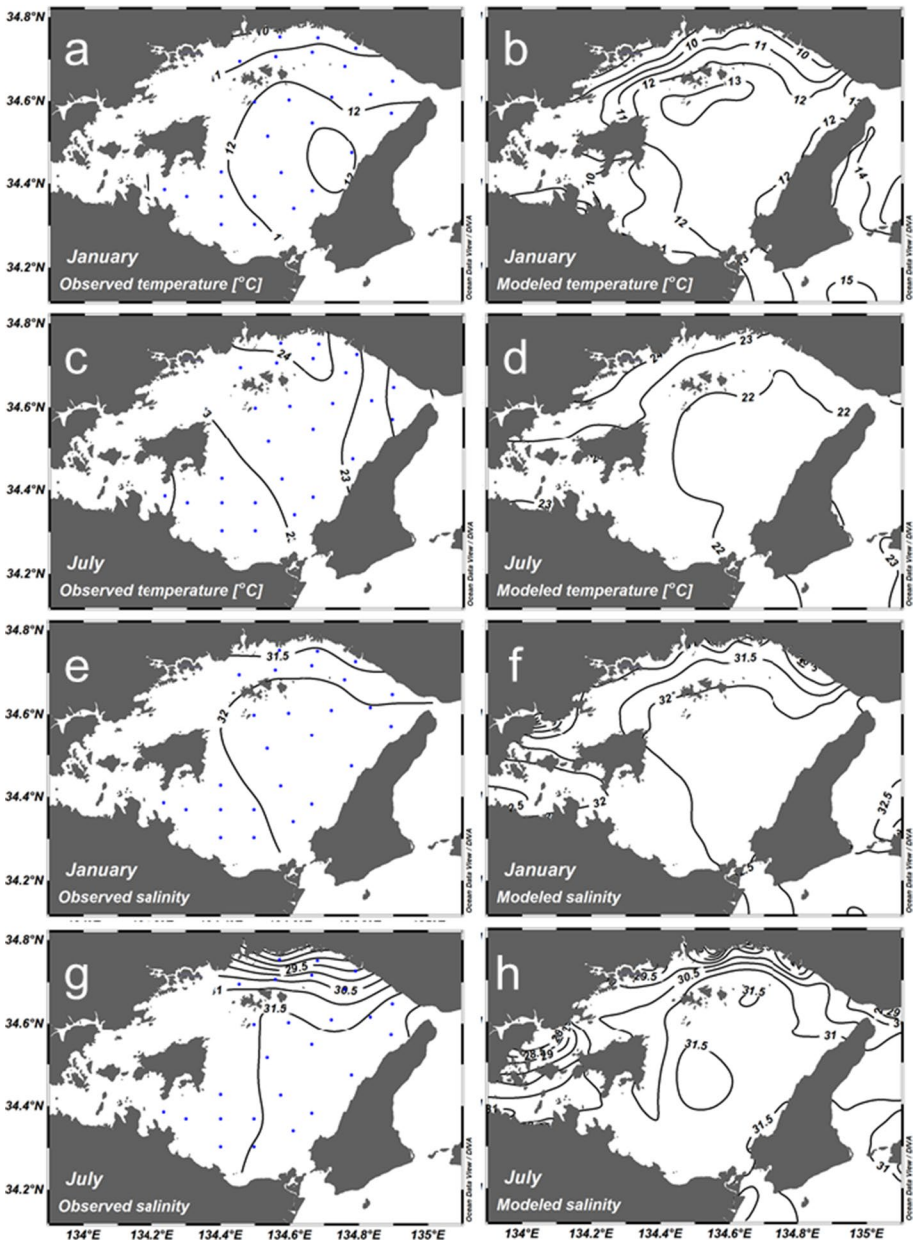

Fig. 4 Spatial distributions of observed and simulation near-surface temperature (**a**–**d**) and salinity (**e**–**h**) in January and July in Harima-Nada. The contour interval is 1 °C and 0.5 for temperature and salinity, respectively (color figure online)

of vertical temperature profiles between modeled and observed data in July at stations 1–5 is shown in Fig. 6. The observed temperature profiles indicate strong stratification in most stations, except in station 3. The large standard deviation mostly occurred below the depth 30 m, suggesting the inter-annual variability of the BCW. The results clearly show that the model successfully reproduces observed temperature profiles at stations 1, 2, and 5. However, at stations 3 and 4, the model exhibits similar temperatures near the surface layer, gradually large in the deeper layers, which suggests that the model establishes an intensified BCW in those areas compared to the observation. Although the BCW in the model tends to be intensified, the model effectively reproduces the observed temperature and salinity patterns and values in the study area.

3.1.3 Surface current fields

The mooring surface current velocity data were collected at various times between 1972 and 1992 during the months of April and June to September. The duration of mooring period was from 2 weeks to a month, and observed intervals were from 5 to 60 min. As process the data, a 25-h running mean is applied to remove tidal signals and then averaged during mooring period. The results of the mooring data analysis are presented in Fig. 7, showing current field in April and June to September, representing

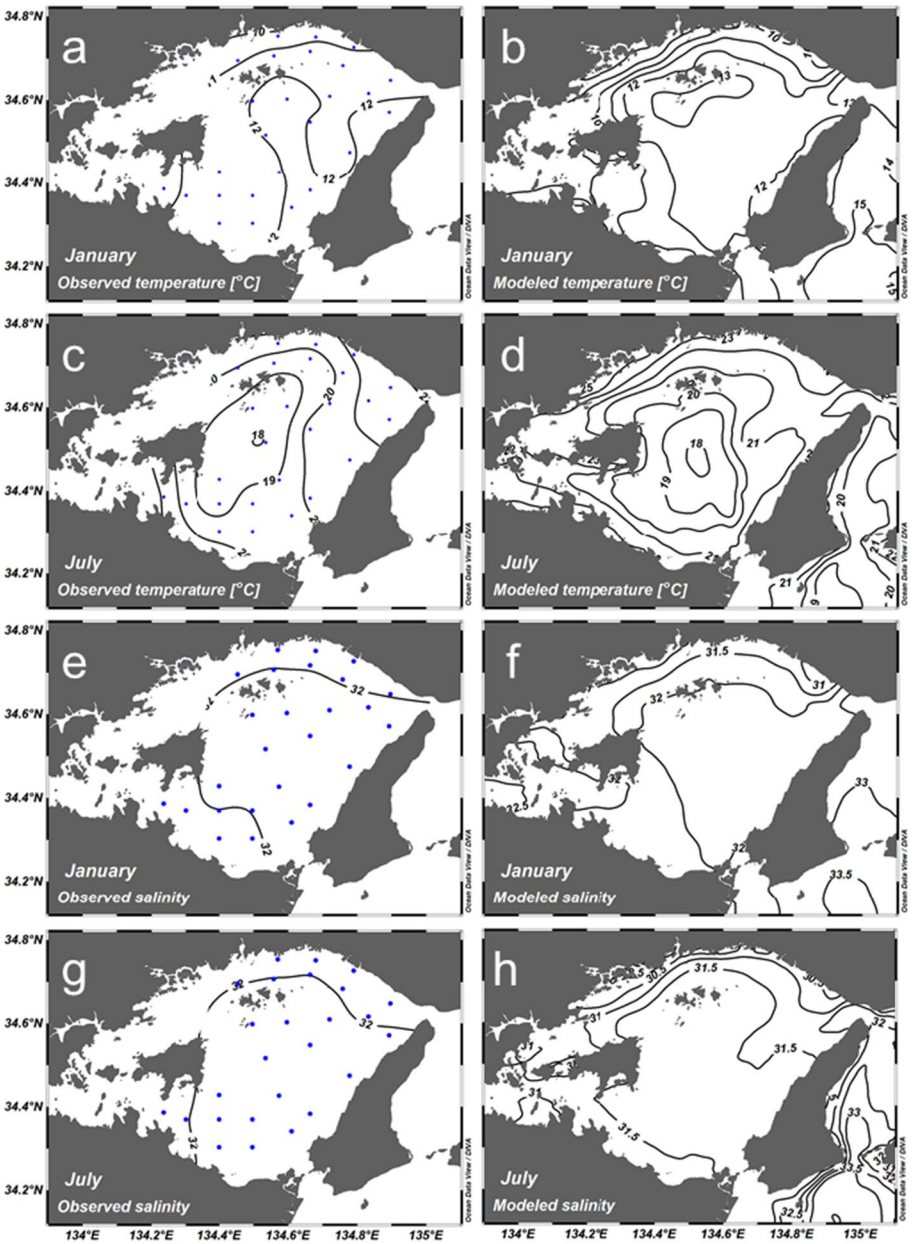

Fig. 5 The same as Fig. 4, but for near-bottom. The contour interval is 1 °C and 0.5 for temperature and salinity, respectively (color figure online)

the spring and summer seasons. In spring, the appearance of anticyclonic eddy-like patterns near the Akashi Strait is observed, which is also reflected in the modeled results shown in Fig. 8a. The magnitude of the surface currents in the observations is in the range 0.09-0.11 m s^{-1}, which is a little stronger than the modeled results (0.04–0.07 m s^{-1}). In summer, the observations reveal the presence of cyclonic eddy in the central basin of the Harima-Nada, as well as the southwestward currents near the Akashi Strait. The modeled results successfully reproduce these features as shown in Fig. 8a. The magnitude of the surface current near the Akashi Strait in the model (0.15 m s^{-1}) is constituent with that in the observations (approximately 0.17 m s^{-1}). As for the magnitude of cyclonic eddy, modeled currents (0.2 m s^{-1}) are stronger than the observed current (0.06–0.13 m s^{-1}). The coastal currents along the northwestern and northern coast of the Harima-Nada predominantly flow in a northeastward direction with an average magnitude of 0.9 m s^{-1} in the observations. However, the modeled results exhibit northeastward currents along the northwestern coast and southwestward currents along the northern coast. The magnitude of the modeled currents is relatively stronger near the northern coast compared to the observations. These inconsistencies in patterns and magnitudes between the modeled and observed results may be attributed to the difference in the observation period (year-by-year) compared to the long-term averaged data used in the model simulations.

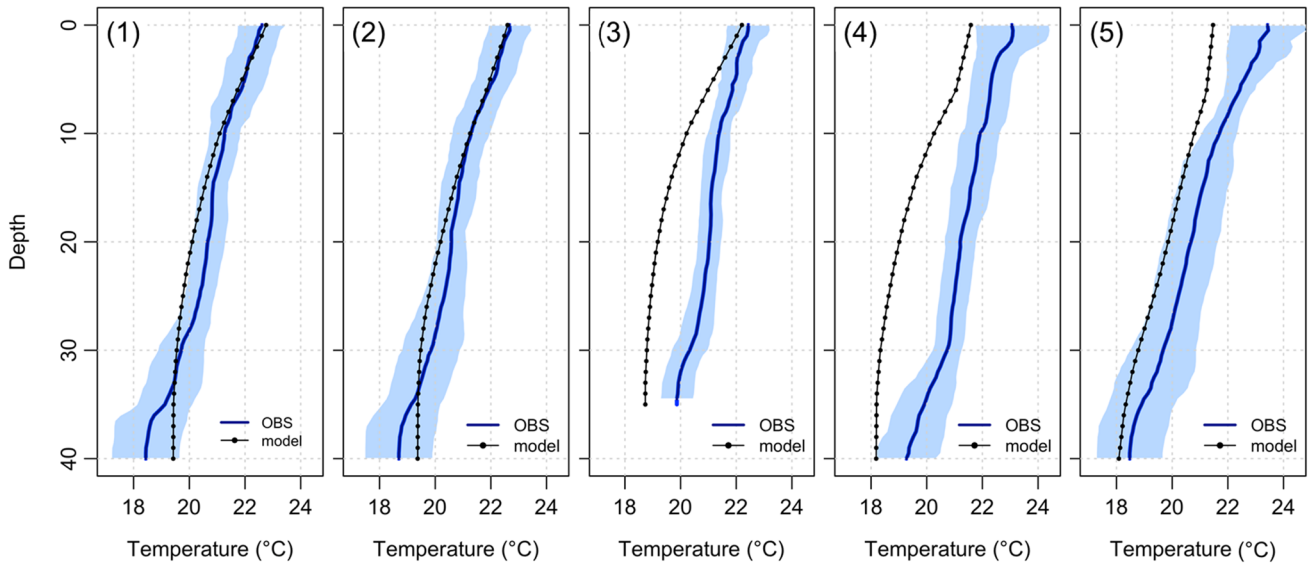

Fig. 6 The vertical profiles of temperature in July, comparing the model results (black lines with dots) and long-term observations (blue lines). The shaded areas indicate the standard deviations of observation data (see Fig. 1b for the location of stations 1 to 5) (color figure online)

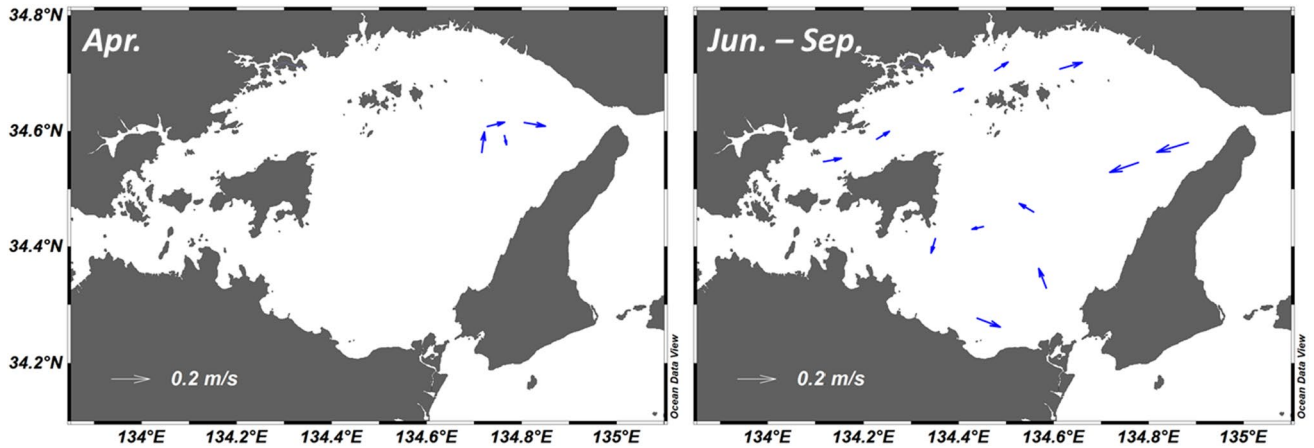

Fig. 7 Mooring observation current data at near-surface layer during 1972–1992. The left panel shows the moored data during April and the right panel shows the moored data during June to September (color figure online)

Nevertheless, the model generally performs well in capturing the observed surface currents in the Harima-Nada.

3.2 Seasonal variation in the hydrographic field

In this section, we describe the seasonal variation in the surface and bottom current fields and the horizontal and vertical distributions of temperature and salinity. To remove high-frequency signals such as tidal currents, a tide-killer filter was applied to the model results, and the resulting values were averaged monthly.

3.2.1 Spatial and seasonal variation in current fields

Seasonal variation in the near-surface and near-bottom current fields is shown in Fig. 8, in which January, April, July, and October are defined as the representative months for winter, spring, summer, and autumn, respectively. In January, southeastward currents are dominant at the surface across the entire Harima-Nada, which might be related to the winter monsoon wind. Water flows into Harima-Nada from Osaka Bay through Akashi Strait, and a cyclonic eddy was present west of the strait. Meanwhile, water flowed out to Kii Channel through Naruto Strait. Current speeds

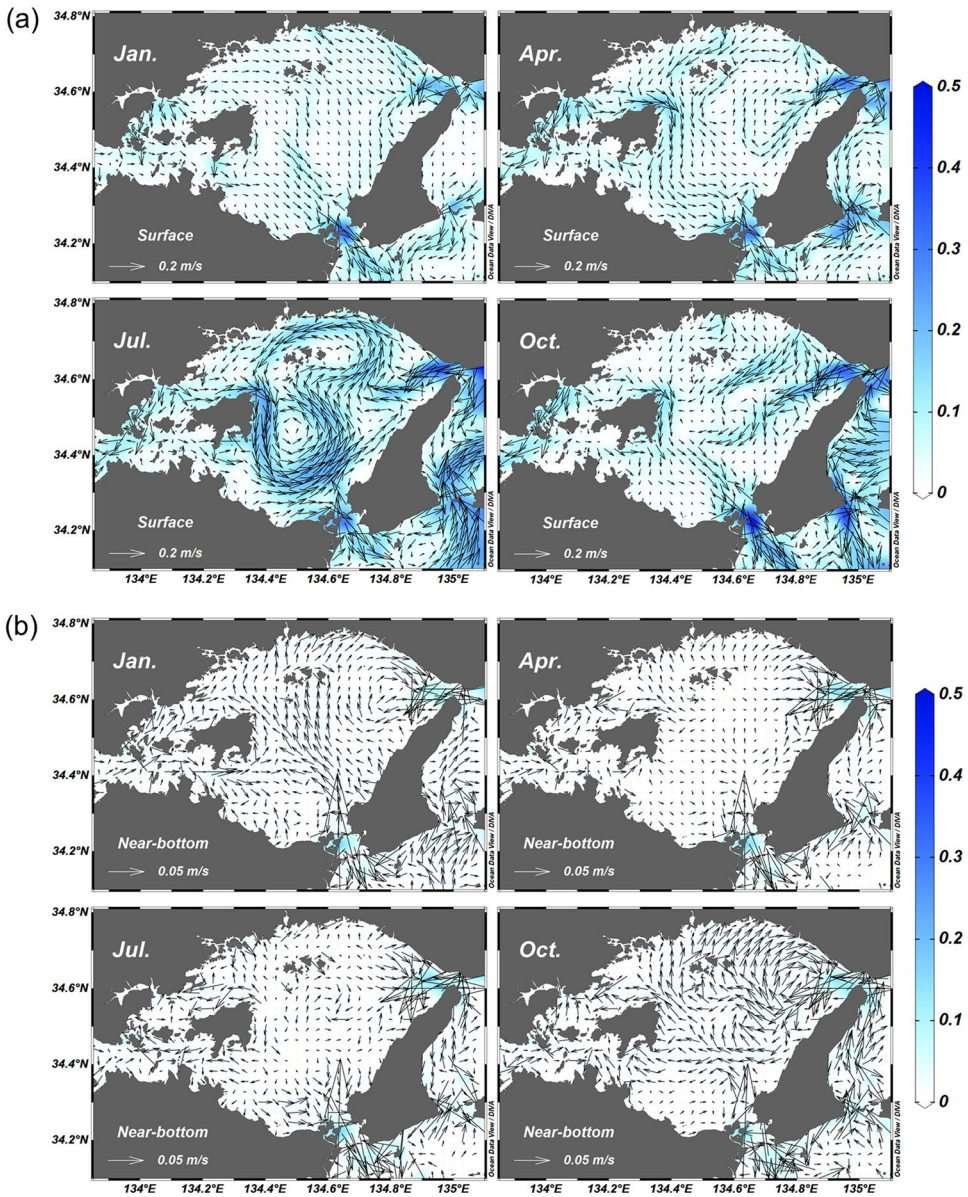

Fig. 8 Monthly average of simulated surface (**a**) and near-bottom (**b**) current distributions in January, April, July, and October. The arrow represents current vectors and color represents current magnitude (unit: m s^{-1}) (color figure online)

were relatively weak (0.05–0.10 m s^{-1}) in the central part of Harima-Nada. In April, westward coastal currents appeared along the northern coast, while strong southward and southeastward currents were found along the eastern coast of Shodoshima Island and in the southern part of Harima-Nada, respectively. The current patterns around Akashi and Naruto Straits were similar to those in the winter season. Cyclonic and anticyclonic eddy-like patterns are likely present in the basin and northern part of Harima-Nada, respectively. In July, a cyclonic eddy was well-developed in the central part of the basin, with a maximum speed of 0.25 m s^{-1}. A strong westward coastal current occurred along the northern coast, and the current exhibited counter-clockwise circulation in the northern part of Harima-Nada. In October, southeastward current was present in the central basin, along with southwestward currents in the northeastern part of the basin and southward currents along the eastern coast of Shodoshima Island. In addition, a well-developed cyclonic eddy was found in the southern part of Akashi Strait in this season.

Figure 8b shows the horizontal distributions of near-bottom currents in January, April, July, and October. In January, upwind currents (northwestward currents) were clearly present throughout the study area, and were stronger in the deeper region than in the shallower region. In Akashi Strait, the current flowed into Harima-Nada, similar to the near-surface current. Moreover, an anticyclonic eddy-like pattern was present in the northeastern part of Harima-Nada. In April, the near-bottom current was relatively weak compared to other seasons and no distinct circulation patterns were

noted. Divergent currents appeared in the northern part of the basin in this season. The near-bottom current was similar in July to the spring season, except that divergent currents were present in the central basin, where a cyclonic eddy occurred in the surface layer. In October, current speeds were relatively strong compared to other seasons. Downwind currents appeared in the southern part of the basin, while upwind currents were found in the northern part of the basin. An anticyclonic eddy-like pattern with a speed of 0.03 m s^{-1} was apparent in the northeastern part of Harima-Nada. In addition, a cyclonic eddy appeared south of Akashi Strait, where a cyclonic eddy also occurred at the surface.

3.2.2 Seasonal variation in water temperature and salinity

In general, spatial differences in water temperature at the surface were small across Harima-Nada regardless of seasonal changes. On the other hand, salinity varied both seasonally and spatially. Water temperature was lowest during winter (8 °C), gradually increased during spring, and was highest in summer (27 °C). On the other hand, salinity was highest in winter (32), gradually decreased during spring, and was lowest in summer (30.5). Thus, cool and saline waters were present in winter due to cooling of the sea surface and low river discharge. On the other hand, in summer, the sea surface gained heat from the atmosphere and higher river discharge was supplied, causing a warm and less saline water mass to form.

Water temperature and salinity around the straits were well-mixed throughout the year due to strong tidal mixing. On the other hand, the vertical structure of water masses in the basin showed seasonal variation. We plotted the vertical distribution of temperature, salinity, and density along section A′–B′ (shown in Fig. 1c) in January, April, July, and October (Fig. 9). In winter (January), the vertical distributions show well-mixed structures of temperature, salinity, and density. Cool (12 °C) and saline water (32) results in high density (1024.5 kg m^{-3}) in the basin. During spring (April), slight vertical gradients of temperature, salinity, and density form, which become pronounced in summer. In summer (July), the water is strongly stratified and a cold dome is present at the bottom of the basin. The temperature ranges from 17.8 to 21.6 °C, and the salinity ranges from 31.6 to 31.9, from the bottom to the surface. The vertical gradients of salinity are relatively weak compared to those of temperature, and thus the vertical gradient of density is largely driven by temperature. In autumn (October), water temperature rises to 25 °C and the vertical gradient of temperature nearly disappears. On the other hand, salinity is relatively stratified, and therefore salinity is reflected in the vertical density gradient. Overall, the surface warm pool and bottom cold dome are well established in summer due to the difference between surface and bottom water temperatures of approximately 3.8 °C.

3.3 Formation of HNBCW and a cyclonic eddy in central Harima-Nada

The summer features described in the previous section demonstrate that the HNBCW was present in the lower layer and a cyclonic eddy occurred in the surface layer above it. Therefore, we explore the occurrence of the HNBCW and its relationship with the cyclonic eddy in this section.

3.3.1 Formation of HNBCW and structures

Figure 10 shows the time series of observed and modeled temperature in the BCW region. Stratification began in spring due to sea surface heating, became well-stratified in summer due to intensified surface heating and weak winds, and then decayed in early autumn due to surface cooling. Based on the observation data, the water temperature at the surface increased from 11.2 to 26.7 °C, and from 10.4 to 21.4 °C at the bottom. Hence, there was surface temperature increase of 15.5 °C, and a bottom temperature increase of 11.0 °C. The temperature difference between the surface and bottom layers reached 5.2 °C in mid-August (Fig. 10a). The rate of temperature increase during the summer season was approximately 3.9 °C $month^{-1}$ at the sea surface and 2.8 °C $month^{-1}$ at the bottom. On the other hand, the water temperature derived from the model results, revealed that at the surface, (bottom) increased from 10.2 (9.4) °C in early April to 25.3 (22.2) °C in August; increase of surface and bottom water temperature is 15.1 °C and 12.8 °C, respectively. The difference in water temperature between the surface and bottom layers reached 3.2 °C in mid-August. The rate of change in water temperature from mid-autumn to early spring is similar between the surface and bottom layer, but differs from the rate in mid-spring to early autumn. In spring, the rate of increase in water temperature is 0.10–0.20 °C day^{-1} at the surface and 0.05–0.10 °C day^{-1} at the bottom, leading to the development of stratification. Conversely, the rate rapidly decreases (by approximately 0.10–0.20 °C day^{-1}) in the surface layer from late summer to early autumn. Meanwhile, the rate in the bottom layer increases (by approximately 0.6 °C day^{-1}) in late summer and decreases during early autumn, causing stratification to disappear. Accordingly, the rate of increase in the surface layer is accelerated in spring, while the bottom layer does not show this trend.

We selected July to represent the HNBCW in summer because the difference in water temperature between the surface and bottom is relatively constant than in August. Moreover, we defined the boundary of the HNBCW as the 19 °C isotherm to isolate the BCW mass from the

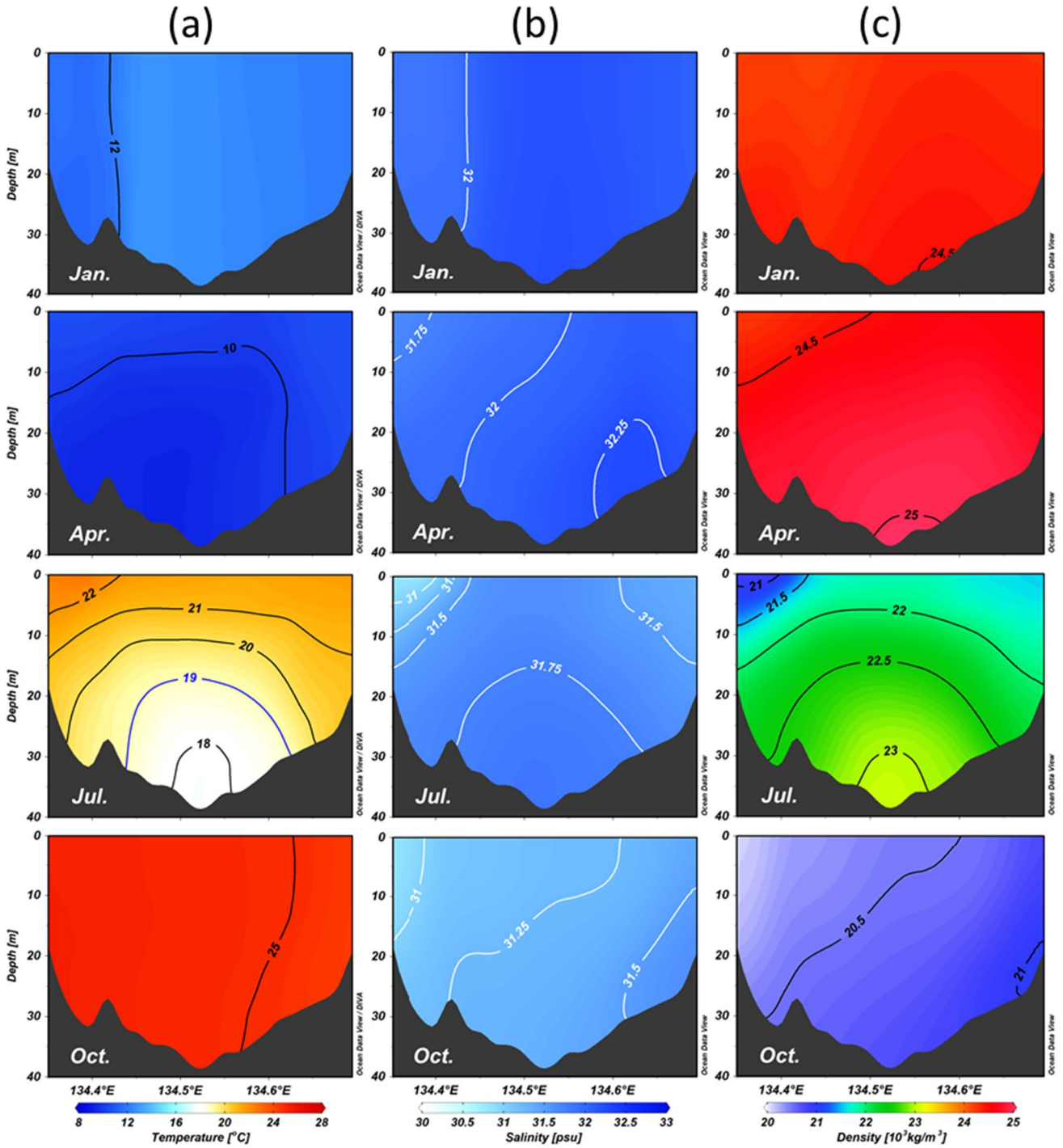

Fig. 9 Vertical distributions of simulated temperature (**a**), salinity (**b**), and Sigma-T (**c**) along a section A′–B′ (see Fig. 1c for the location of section A′–B′) in January, April, July, and October. The blue line of the 19 °C isotherm in ′ is used to define the Harima-Nada bottom cold water (color figure online)

surrounding water. The area of the HNBCW is approximately 21 km × 30 km in the zonal and meridional directions, respectively (Fig. 5d), with a maximum (average) thickness of around 21.5 (10.5) m (July in Fig. 9). The HNBCW is located in the central deep portion of the basin below 15 m. The temperature increasing rate during the summer season is approximately 3.8 °C month^{-1} at the sea surface and 3.2 °C month^{-1} at the bottom.

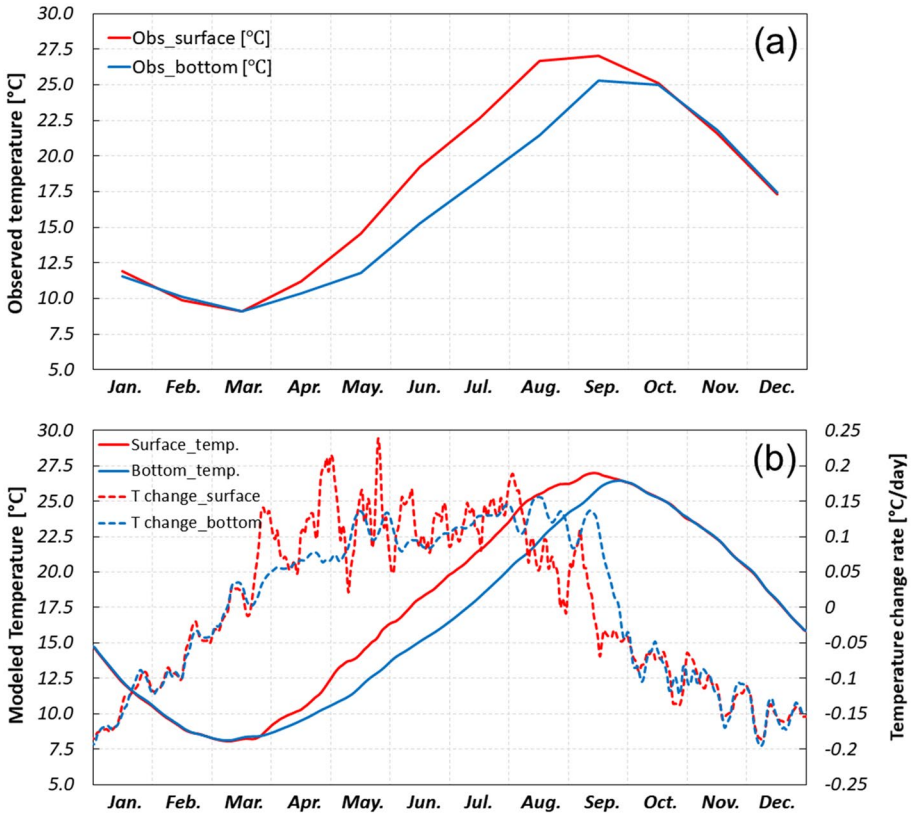

Fig. 10 **a** Time series of monthly-average observed temperature from stations 1 to 2, and **b** daily-average modeled temperature in the HNBCW region. Red solid lines represent the surface temperature, and the blue solid lines represent the bottom temperature. In **b**, right axis shows the temperature (T) change rate (°C day^{-1}) for the surface (red dashed line) and bottom (blue dashed line) layers of the HNBCW (color figure online)

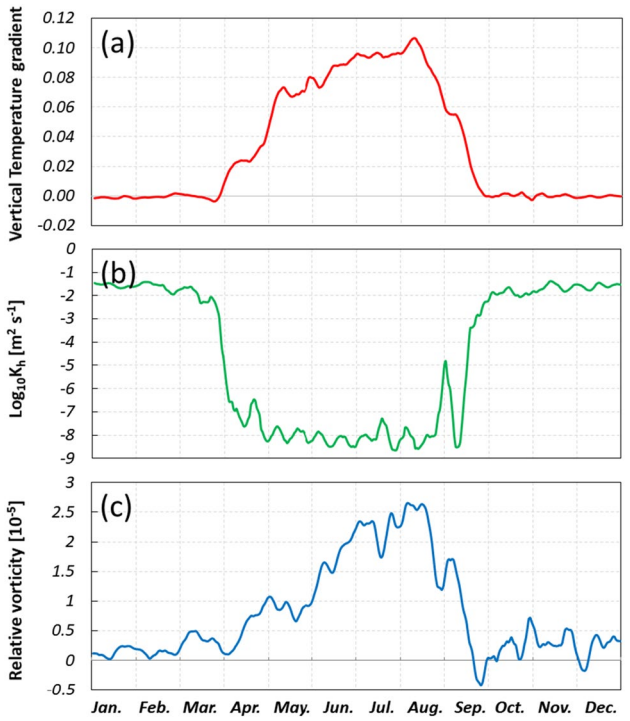

Fig. 11 Time series of daily-average vertical temperature gradient (**a**), vertical diffusivity coefficient above the HNBCW (**b**), and relative vorticity at the surface layer (**c**). The lines are 7-days moving averaged (color figure online)

3.3.2 Mechanism of HNBCW formation and its relationship with cyclonic eddy

Figure 11 shows the time series of daily averaged vertical temperature gradient, vertical diffusivity coefficient, and relative vorticity. The vertical temperature gradient is nearly 0 °C m^{-1} from late autumn to early spring, gradually increases to about 0.10 °C m^{-1} in summer, and then rapidly decreases to nearly 0 °C m^{-1} in early autumn (Fig. 11a). The vertical diffusivity coefficient (K_h) above the HNBCW (approximately 15 m in depth) shows an apparent response to the well-mixed and stratified seasonal patterns, with large values in winter (2×10^{-2} m^2 s^{-1}) that gradually decrease in spring to summer and then increase again in autumn. The vertical diffusivity coefficient in summer ranges from 2×10^{-9} to 10×10^{-9} m^2 s^{-1} (Fig. 11b). Meanwhile, relative vorticity showed the similar pattern to the vertical temperature gradient, when the vertical temperature gradient reached its peak (Fig. 11c). Strong stratification prevents downward heat transport from the sea surface to the bottom layer, which results in small vertical diffusion above the HNBCW. The relationship between the vertical temperature gradient and vertical diffusivity suggests that the HNBCW is controlled by the vertical diffusion process.

In general, heat transport in water is governed by the processes of advection and diffusion. Water temperature differs between the BCW and the surrounding water. To clarify

the processes driving heat transport inside the HNBCW, we calculated the contribution of each process to the change in water temperature. The temporal change in water temperature in the hydrodynamic model is calculated with the following equation:

$$\frac{\partial T}{\partial t} = \mathrm{AdvT} + \mathrm{VdfT} + \mathrm{HdfT}, \tag{1}$$

where $\frac{\partial T}{\partial t}$ is the temporal change in water temperature in the BCW, AdvT is the sum of the advection term, VdfT is the vertical diffusion term, and HdfT is the horizontal diffusion term. A tide-killer filter was applied to the hourly results for each term of Eq. (1) and other parameters, and integration was performed over 24 h.

Figure 12 shows daily averaged heat transport processes at the center of HNBCW from January to December based on Eq. (1). Note that the horizontal diffusion term is relatively small compared to the advection and vertical diffusion terms, and thus is not shown here. Increase of water temperature (°C day^{-1}) is quite small in winter and relatively large in summer. In summer, the rate of increase in water temperature between the surface and 30 m depth is larger than that below 30 m depth. Moreover, variation in the increase rate of water temperature corresponds to the spring–neap tidal cycle (Fig. 12a). Advection term at depths of 15–30 m is positive and accelerates from July to September, indicating that the advection process transfers heat to the upper part of HNBCW (Fig. 12b). The vertical diffusion term is consistently positive during the summer season. From the surface to 15 m in depth, vertical diffusion is greater than below 15 m, suggesting that downward heat transport from the sea surface to the HNBCW is limited by the thermocline (Fig. 12c).

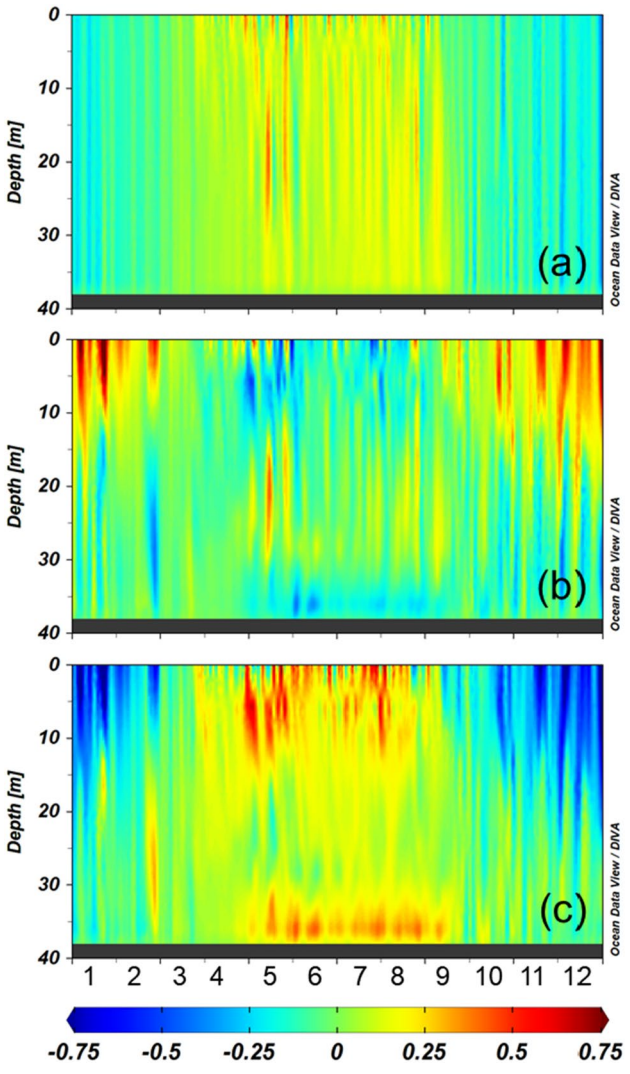

Fig. 12 Daily-integrated of each term from Eq. (1). **a** Daily increase in water temperature (°C), **b** sum of the advection term (°C day^{-1}) and **c** vertical diffusion term (°C day^{-1}) (color figure online)

As noted in the previous section, the HNBCW is associated with an overlying surface cyclonic eddy, and the vertical temperature gradient has a relationship with relative vorticity. Here, we investigated the generation of this cyclonic eddy and its relationship with the HNBCW. As stratification begins in spring and ceases in autumn, the monthly mean normal velocity was illustrated along with water temperature from April to September (Fig. 13). Stratification formed in April and accelerated toward summer due to both surface heating and increased river discharge, which induces a large horizontal pressure gradient between areas to the north and south of Harima-Nada. To maintain quasi-stable flow, this horizontal pressure gradient force is balanced by the Coriolis force. Consequently, a cyclonic eddy is generated in the surface layer that isolates a dome of cold bottom water from the previous winter. This generation mechanism is similar to that of the anticlockwise eddy in the eastern part of Hiuchi-Nada described by Guo et al. (2004) and also explains the formation of a cyclonic gyre in the western Irish Sea (Hill et al. 1997). Warming accelerates toward summer (July to August), causing the surface layer to become warmer than the bottom layer due to limited heat transport at the thermocline. In consequence, the cyclonic eddy becomes stronger at the surface layer and the dome of cold bottom water becomes sharper (Hill 1993). The cyclonic eddy is sustained through the summer season and gradually changes in response to sea surface cooling and well-mixed water during autumn.

3.4 Sensitivity analysis for the HNBCW and cyclonic eddy

3.4.1 Influences of heat flux and river discharge

HNBCW developed in summer and was controlled by heat transport through the processes of advection and vertical diffusion. To investigate the response of the HNBCW to dynamic factors, we conducted numerical sensitivity

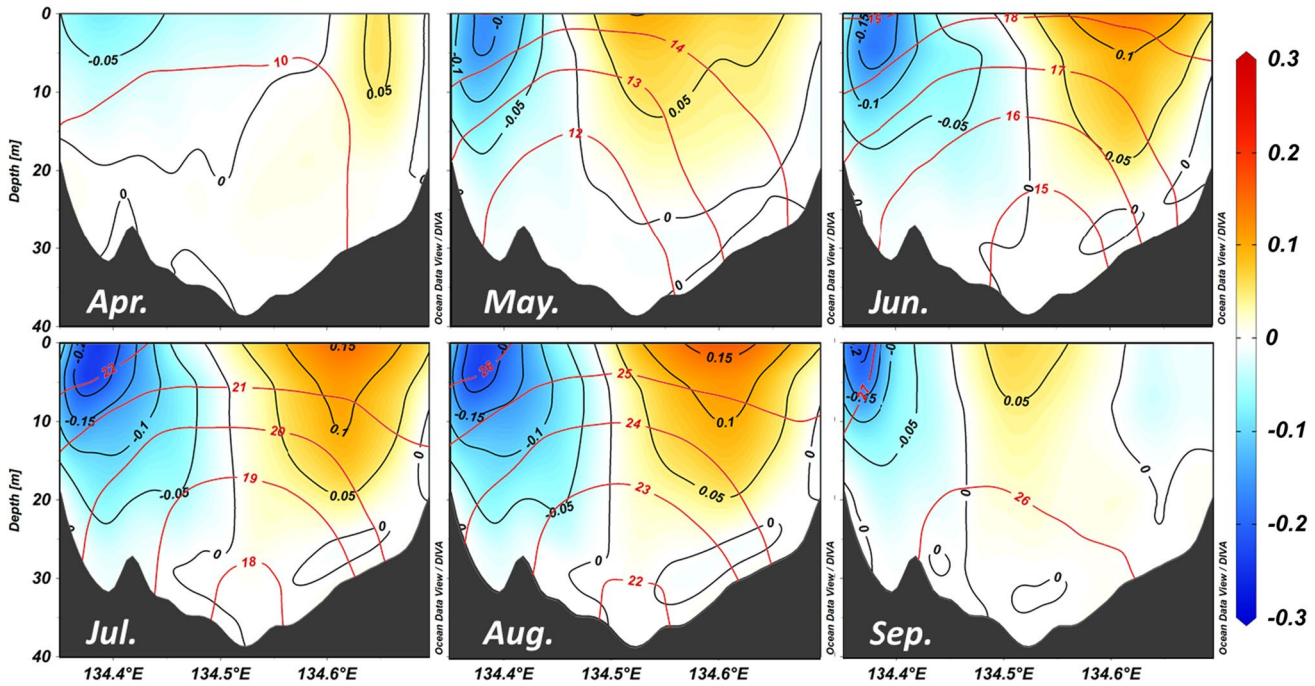

Fig. 13 Monthly mean cross-section distributions of normal velocity (m s^{-1}) along a section A′–B′ (see Fig. 1c for the location of section A′–B′) from April to September (color with black contour). Additionally, water temperature contours are shown by red lines with red labels (color figure online)

Table 2 Sensitivity experiments and conditions

Experiments	Conditions
Case 1	River discharge increased by 30%
Case 2	River discharge decreased by 30%
Case 3	The surface heat loss in the previous winter increased by 20%
Case 4	The surface heat loss in the previous winter decreased by 20%
Case 5	The surface heat gain in spring increased by 10%
Case 6	The surface heat gain in spring decreased by 10%

experiments (Table 2). We investigated only the influences of river discharge and air–sea heat flux, not local winds. Discharge reached its peak in summer and played an important role in density-driven circulation. Meanwhile, air–sea heat flux generally plays a significant role in circulation in coastal sea areas and responds to the formation of a BCW mass. However, local wind stress is relatively weak and might not influence circulation in summer.

In general, the sea surface loses heat in winter and gains heat in spring and summer. To determine the effects of air–sea heat flux on the HNBCW under diverse conditions, we increased and decreased air–sea heat flux over Harima-Nada in winter (December to February) and spring (April to June). In addition, to determine the effects of river discharge, we increased and decreased the discharge of each river from May to July. Percentages given in Table 2 for each sensitivity experiment are based on the long-term variation in each factor and season. The model was run for 3 years as control case and then apply each conditions as shown in Table 2. The results were saved at an hourly for 4th year. Before further analysis, a 25 h running mean was applied to the results to remove tidal signals.

To quantify the response of HNBCW, we used the percentage sensitivity coefficient (% coefficient), which can be calculated with the following equation:

$$\%\ \text{coefficient} = \left[\frac{X_{\text{case}} - X_{\text{control}}}{X_{\text{control}}}\right] \times 100, \tag{2}$$

where subscript case and control represent the average values from one of the sensitivity experiments and the climatology simulation, respectively, and x is the variable for water temperature, thickness, or the area of HNBCW enclosed by a specific isothermal (19 °C, July in Fig. 9).

Table 3 Percent of sensitivity coefficient for each variable in the sensitivity experiments

Experiments	Sensitivity coefficient (%)		
	Temperature	Thickness	Area
Case 1	+0.03	−2.31	+1.10
Case 2	−0.04	+2.88	−0.58
Case 3	−0.57	+8.06	+13.87
Case 4	+0.49	−7.17	−19.65
Case 5	+0.26	−5.83	−14.86
Case 6	−0.32	+7.53	+13.06

Table 3 shows the percentage sensitivity coefficient for each experiment in terms of water temperature, thickness, and area of the HNBCW. Positive values indicate that the value for the sensitivity experiment is greater than for the control case and negative values indicate that it is below the control case value. The sensitivity coefficient in terms of water temperature was most prominent in Case 3 and Case 4, followed by Case 6 and Case 5. This suggests that air–sea heat flux during winter plays a significant role in determining HNBCW water temperature. In terms of thickness, the sensitivity coefficient was relatively high in cases involving air–sea heat flux, indicating that both spring and winter air–sea heat fluxes have equally important and influences on HNBCW thickness. The sensitivity coefficient for thickness in river discharge cases was comparable but lower than those in air–sea heat flux cases. Regarding HNBCW area, Case 4 had the highest sensitivity coefficient, followed by Case 5, Case 3, and Case 6. This implies that air–sea heat flux has a greater impact on HNBCW area compared to river discharge. Conversely, the sensitivity coefficients in altered river discharge cases (Case 1 and Case 2) were lower than in other cases, indicating that river discharge does not have a direct impact on the HNBCW.

Cold water from the previous winter was trapped in the bottom layer after the onset of the warming season. Thus, air–sea heat flux change in winter is the most significant factor controlling the water temperature of the HNBCW. These changes also had a substantial impact on the thickness and area of HNBCW. Similarly, air–sea heat flux during spring has a comparable effect on the thickness and area of HNBCW as in winter. The warming season initiates in April, leading to an increase in water temperature facilitated by vertical diffusion and advection processes. As Harima-Nada is a shallow coastal sea, there is substantial heat diffusion from the sea surface into the HNBCW through downward heat transport. Therefore, variations in the air–sea heat flux during spring are crucial in driving changes in the water temperature of the HNBCW. Although air–sea heat fluxes in winter and spring play different roles in the formation of HNBCW, no significant difference in the cyclonic circulation above the HNBCW was observed.

River discharge is another factor influencing circulation in the summer season. The balance between the horizontal pressure gradient and the Coriolis force generates geostrophic flow. Therefore, changes in river discharge affect circulation associated with the HNBCW below the cyclonic eddy. Figure 14 shows the vertical distributions of water temperature (a) and normal velocity (b) in July for the control case, as well as cases of increased (Case 1), and decreased (Case 2) river discharge. Additionally, the red contour line shown in Case 1 and Case 2 is the contour of the Control Case. An increase in river discharge strengthens density-driven currents, causing a relatively strong horizontal current that can transport heat from surrounding warm water to the HNBCW, which increases water temperature within the HNBCW. Moreover, the thermocline above the HNBCW shifted downward due to the strong cyclonic eddy at the surface layer; the thickness of HNBCW is smaller and its area is larger than in the control case. The case of decreased river discharge showed the opposite results as the case of increased discharge, with a weaker density-driven current resulting in weak horizontal advection of heat transport. Consequently, cooler water temperature within the HNBCW, which is of greater thickness and smaller area compared to the control case, is predicted. However, the influences of river discharge minimally contributed to the HNBCW because the boundary of 19 °C isotherm was deeper than the effect of cyclonic eddy, changes in river discharge play small rule in HNBCW.

3.4.2 Influences of topography

Generally, stratification develops during the warming season in areas where the tidal current is weak and the water is relatively deep, e.g., basin and shelf areas. The transition from mixed to stratified regimes is associated with tidal fronts. Tidal fronts occur along the critical contour line of $\log_{10}(H/U^3)$, where H is the water depth and U is the amplitude of the M_2 tidal current, with a critical value of 2.5–3 in the SIS (Yanagi 2003). The BCW becomes trapped after the onset of stratification beneath the thermocline in topographic depressions. In addition, the complex topographic features of Harima-Nada affect the BCW mass and cyclonic eddy. Therefore, we conducted two numerical experiments with variation in bottom topography. First, we artificially modified the bottom topography to remove Shodoshima Island (Case 7), and second, we set a fixed depth of about 30 m across the entire calculation domain (Case 8). The hydrodynamic model was run again with the same forcing as the control case, changing only the bottom topography. The results are shown in Fig. 15.

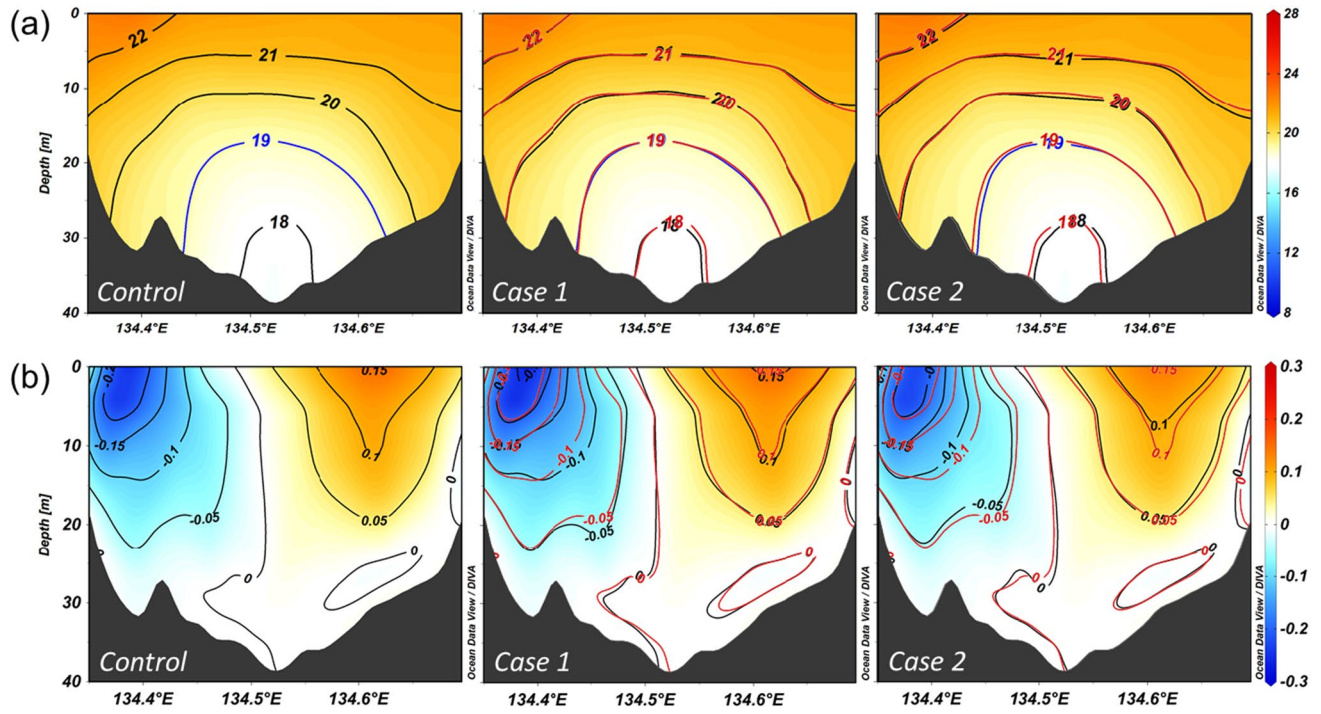

Fig. 14 Cross-section distributions of temperature (°C) (**a**) and normal velocity (m s^{-1}) (**b**) along a section A′–B′ (see Fig. 1c for the location of section A′–B′) for the control case, increased river discharge (Case 1) and decreased river discharge (Case 2) in July. The red contour lines in Case 1 and Case 2 represent the contour line of the Control Case (color figure online)

The distribution of the surface current field shows that Case 7 is similar to the control case, with a cyclonic eddy at the center of the bay and counter-clockwise circulation in the northern part of the bay. However, the cyclonic eddy is relatively large compared to the control case, occupying the entire basin (Fig. 15b). On the other hand, the current field in Case 8 shows a markedly different pattern, in which the cyclonic eddy in the central part is unclear and the counter-clockwise circulation in the northern part is extended (Fig. 15c). Cyclonic eddy variation might be related to the change in $\log_{10}(H/U^3)$ and position of the tidal front, as the cyclonic eddy occurs around the contour of 3–3.5 (Fig. 15d). Without Shodoshima Island (Case 7), the tidal front shifted westward toward Bisan-Seto, indicating that stratification was enhanced, and as a result, the cyclonic eddy was relatively large (Fig. 15e). Flat topography (Case 8) affects the residual currents and water exchange among bays. As the water depth at the straits becomes shallower, tidal currents around the straits in Case 8 become stronger than in the control case. Thus, no geostrophic flow is generated and no cyclonic eddy forms, although the distribution of $\log_{10}(H/U^3)$ is quite similar to the control case (Fig. 15f). In conclusion, topographic features play an important role in generating the circulation pattern of Harima-Nada.

The BCW mass in Case 7 is relatively large and cold compared to the control case and is associated with the shape of the cyclonic eddy above it (Fig. 15h). By contrast, the BCW mass in Case 8 is warmer than in the control case (Fig. 15i). As noted above, a cyclonic eddy is associated with the tidal fronts and occurs with the BCW. Furthermore, heat transport via advection is another important factor affecting the BCW; heat transport from surrounding warm water weakens under weak tidal current regimes. Heat transport via advection is greater in the case with flat topography due to the strong tidal current, and therefore the water temperature is relatively high in that case.

3.5 Comparison of BCW with other coastal areas

BCW masses have been widely reported in shelf and coastal sea areas where tidal mixing is relatively weak. Therefore, we compared the characteristics of several BCW masses, as outlined in Table 4. BCW masses in shelf seas such as the Yellow Sea show small increases in water temperatures (Yu and Guo 2018; Zhu et al. 2018). On the other hand, BCW in coastal seas experiences large temperature increases, including in the Irish Sea (Holt and Proctor 2003; Horsburgh and Hill 2003) and the SIS (Yu and Guo 2018; Zhu et al. 2022). The temperature increase in BCW is mainly controlled by limited heat transport through the thermocline. In the Yellow Sea, where the horizontal extent of BCW is large, the temperature increase is mainly driven by downward heat

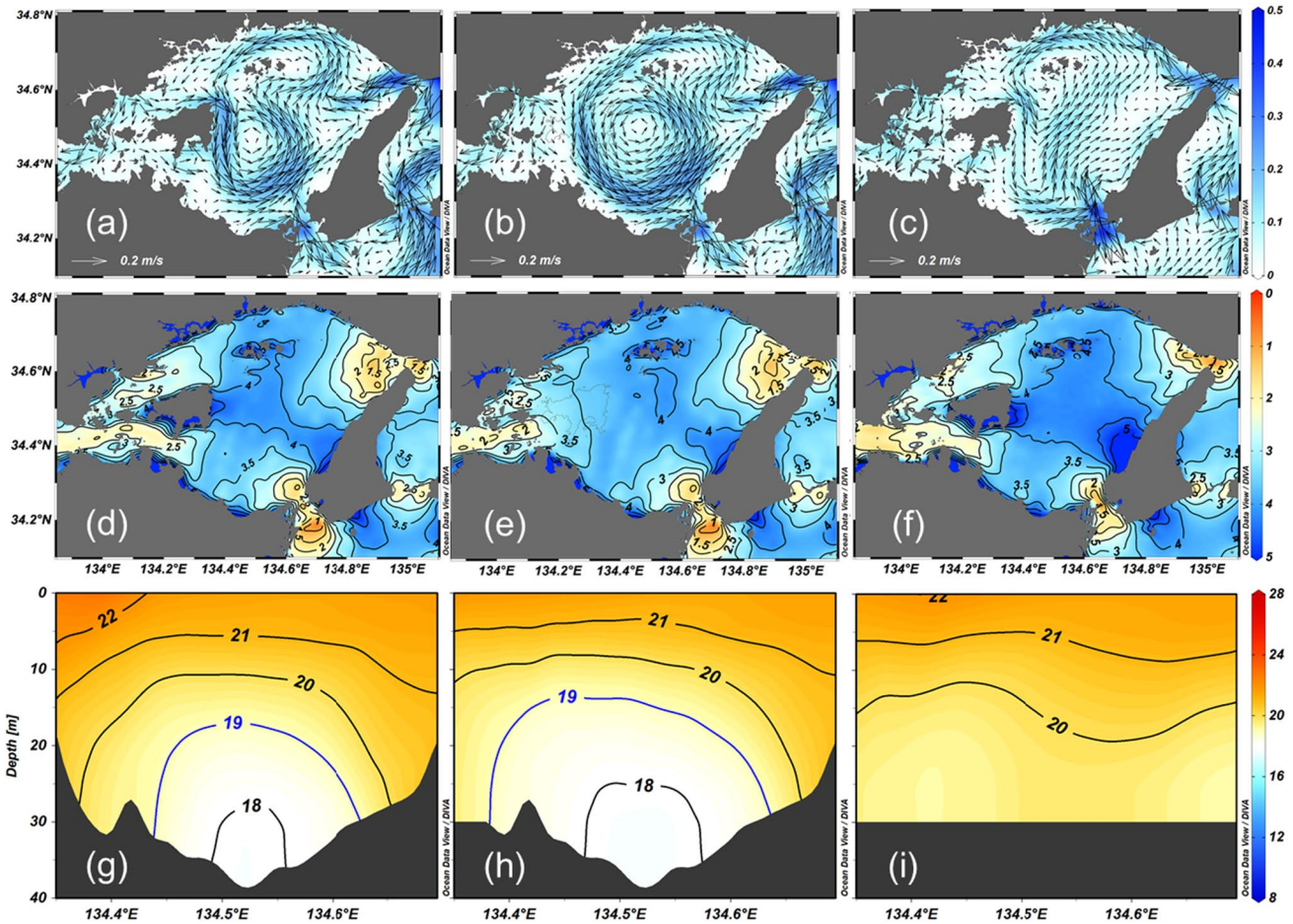

Fig. 15 Distribution of monthly surface current (upper panels), $\log_{10}(H/U^3)$ (middle panels) and cross-section distributions of temperature (lower panels) along a section A′–B′ (see Fig. 1c for location of section A′–B′) in July. Control case is presented in **a**, **d**, and **g**. Without Shodoshima Island (Case 7) presented in **b**, **e**, and **h**. Flat topography (Case 8) presented in **c**, **f**, and **i** (color figure online)

Table 4 Comparison of the BCW with other coastal seas

Coastal seas	Water depth (m)	Temperature increase (°C)	Average thickness of the BCW (m)	Horizontal size of BCW mass (km^2)	Factor of the temperature increase in the BCW	References
Harima-Nada	35	12.8 (Apr–Aug)	10.5	21 km × 30 km	Diffusion, advection	This study
Hiuchi-Nada	20	4–6 (Jun–Aug)	10	16 km × 28 km	Diffusion, advection	Kasai et al. (2007), Yu and Guo (2018)
Iyo-Nada	60	8–10 (Apr–Jul)	30	40 km × 30 km	Diffusion, advection	Yu and Guo (2018)
Irish Sea	100	4 (Apr–Aug)	50	100 km × 100 km	Diffusion, advection	Holt and Proctor (2003), Horsburgh and Hill (2003)
Yellow Sea	70	1 (Apr–Aug)	40	300 km × 300 km	Diffusion	Zhu et al. (2018), Yu and Guo (2018)

transport through vertical diffusion of heat around the thermocline, causing a temperature increase of approximately 1 °C from spring to summer. By contrast, in a coastal sea such as the Irish Sea, where the horizontal area is smaller due to the small area between tidal fronts, the temperature increase is driven by both advection and vertical diffusion from surrounding regions, and therefore the BCW temperature increase is large (4 °C).

In the SIS, the presence of BCW masses has been confirmed in several wide basins, including Iyo-Nada (Kobayashi et al. 2006; Chang et al. 2009; Yu et al. 2016; Yu and Guo 2018), Suo-Nada (Chang et al. 2009; Yu et al. 2016; Yu and Guo 2018), Harima-Nada (Kobayashi et al. 2006; Chang et al. 2009; Yu et al. 2016; Yu and Guo 2018), and Hiuchi-Nada (Ochi and Takeoka 1986; Takeoka et al. 1986; Kasai et al. 2007; Guo et al. 2004; Yu and Guo 2018). These basins have different geographic features, and thus the horizontal and vertical scales of their BCW masses differ. Consequently, these BCW masses have different characteristics. In Iyo-Nada, which is a wide area with deep water, the largest BCW mass in the SIS occurs, which undergoes a temperature increase of about 8–10 °C from spring to summer. The temperature increase in this area is driven by advection from surrounding warm water, which transports heat to the BCW at twice the rate of vertical diffusion (Yu and Guo 2018). Meanwhile, Hiuchi-Nada has the smallest BCW mass in the SIS. This area is a shallow, small region and the tidal current is relatively weak; consequently, the temperature increase is mainly controlled by downward heat transport through vertical diffusion (Yu and Guo 2018). In Harima-Nada, the HNBCW is surrounded by areas of relatively strong tidal mixing around the straits, and thus heat transport from surrounding warm water is relatively large. In addition, Harima-Nada is relatively shallow, and thus downward heat transport through vertical diffusion and redistribution of heat within the HNBCW play significant roles in the rate of increase in water temperature. Accordingly, advection and vertical diffusion play comparable roles in warming the HNBCW.

4 Conclusion

Physical processes in Harima-Nada were investigated based on a high-resolution, three-dimensional numerical model. Seasonal variations in currents and hydrographic fields were examined in this study. Summer features, e.g., BCW and cyclonic eddy, were explored in terms of their mechanisms and controlling factors. The model accurately reproduces long-term observed hydrographic fields, and the simulated current fields were consistent with the surface observed currents and a previous numerical study in the SIS (Chang et al. 2009). Moreover, observed water temperature in summer revealed the existence of a BCW mass in the basin of Harima-Nada (the HNBCW). Therefore, this model has sufficiently good performance for assessing the temporal and seasonal variation in currents and hydrographic fields in Harima-Nada.

The current field shows seasonal variation in both the surface and near-bottom layers in terms of the circulation pattern and magnitude. In winter, winds play an important role in driving circulation, which is downwind in the surface layer and upwind in the near-bottom layer. On the other hand, density-driven circulation plays a significant role in summer circulation, associated with weak winds and stratification. In addition, a cyclonic eddy is generated in the surface layer of the central Harima-Nada in summer. During transitional seasons (spring and autumn), no dominant pattern is observed due to relatively weak winds. The hydrographic fields show distinct winter and summer structures. In winter, vertically well-mixed water is present throughout the study area due to strong northwesterly winds and sea surface cooling. By contrast, in summer, water is strongly stratified in the basin due to relatively weak winds but is well-mixed at the straits due to strong tidal mixing. Stratification begins in spring due to sea surface heating, accelerates toward summer, and then is destroyed in autumn. The BCW mass develops in summer beneath the thermocline layer, above which the cyclonic eddy occurs.

Cold water from the previous winter becomes trapped in the bottom layer after the onset of the warming season, leading to HNBCW generation in the central Harima-Nada. The pressure gradient in spring drives geostrophic flow, which develops into a cyclonic eddy in the surface layer above the BCW mass. The HNBCW experiences a temperature increase from early spring to summer of about 12.8 °C, while the increase at the surface is about 15.1 °C. These large increases in temperature are compatible with the temperature increase measured in Iyo-Nada (Yu and Guo 2018). Heat transport via advection and vertical diffusion is responsible for the large temperature increase within the HNBCW. The vertical diffusion of heat is limited by the thermocline, resulting in an increase in the temperature within the HNBCW due to redistribution of heat inside this water mass. In addition, advection transports warm water from the surrounding area to the HNBCW in association with the tidal cycle.

Air–sea heat flux is the main factor influencing water temperature and its changes in the HNBCW. Water temperature in the previous winter controls the intensity of the BCW mass. However, variation in the air–sea heat flux in spring affects the HNBCW through the processes of advection and vertical diffusion. Furthermore, topographic features affect the circulation and control the formation of HNBCW. River discharge is another factor affecting water circulation, and thus influencing variation in the HNBCW. Harima-Nada is a small, shallow semi-enclosed coastal sea, and therefore any small change in these dynamic factors can affect water characteristics.

Acknowledgements This research was performed by the Environment Research and Technology Development Fund (JPMEERF20205005) of the Environmental Restoration and Conservation Agency Provided by the Ministry of Environment of Japan. The authors thank Drs. Kuninao Tada, Hitomi Yamaguchi, and Masatoshi Nakakuni of Kagawa University for their research collaboration. Hydrographic data for the

whole Harima-Nada were supported by Hyogo Prefectural Fisheries Department and Kagawa Prefectural Fisheries Department. Data of tidal constituent were supported by Hydrographic and Oceanographic Department. Mooring observation data of currents were provided by the Japan Oceanographic Data Center.

Data availability The datasets generated during the course of this study are accessible upon reasonable request from the collabrorative efforts of the Hyogo Prefectural Fisheries Department and the Kagawa Prefectural Fisheries Department.

Declarations

Conflict of interest The authors declare that they have no known competing financial interests or personal relationships that could have appeared to influence the work reported in this paper.

References

Abe K, Tsujino M, Nakagawa N, Abo K (2015) Characteristic of Si:P:N ratio in bottom water in central Suo-Nada, western Seto Inland Sea. J Oceanogr 71:53–63. https://doi.org/10.1007/s10872-014-0262-4

Abo K, Yamamoto T (2019) Oligotrophication and its measures in the Seto Inland Sea, Japan. Bull Jpn Fish Res Educ Agency 49:21–26

Blumberg AF, Mellor GL (1987) A description of a three dimensional coastal ocean circulation model. In: Heaps NS (ed) Three-dimensional coastal ocean models, vol 4. AUG, Washington DC, pp 1–16

Boesch DF (2019) Barriers and bridges in abating coastal eutrophication. Front Mar Sci 6:1–25. https://doi.org/10.3389/fmars.2019.00123

Chang PH, Guo X, Takeoka H (2009) A numerical study of the seasonal circulation in the Seto Inland Sea, Japan. J Oceanogr 65:721–736. https://doi.org/10.1007/s10872-009-0062-4

Cho YK, Kim K (1998) Structure of the Korea Strait Bottom Cold Water and its seasonal variation in 1991. Cont Shelf Res 18:791–804. https://doi.org/10.1016/S0278-4343(98)00013-2

Guo X, Futamura A, Takeoka H (2004) Residual currents in a semi-enclosed bay of the Seto Inland Sea, Japan. J Geophys Res 109:1–23. https://doi.org/10.1029/2003JC002203

Hill AE (1993) Seasonal gyres in shelf seas. Ann Geophys 11:1130–1137

Hill AE, Brown J, Fernand L (1997) The summer gyre in the Western Irish Sea: shelf sea paradigms and management implications. Estuar Coast Shelf Sci 44:83–95

Holt JT, Proctor R (2003) The role of advection in determining the temperature structure of the Irish Sea. J Phys Oceanogr 33:2288–2306. https://doi.org/10.1175/1520-0485(2003)033%3c2288:TROAID%3e2.0.CO;2

Horsburgh KJ, Hill AE (2003) A three-dimensional model of density-driven circulation in the Irish Sea. J Phys Oceanogr 33:343–365. https://doi.org/10.1175/1520-0485(2003)033%3c0343:ATDMOD%3e2.0.CO;2

Johnson DR, Teague WJ (2002) Observations of the Korea Strait bottom cold water. Cont Shelf Res 22:821–831. https://doi.org/10.1016/S0278-4343(01)00099-1

Kaneda A, Takeoka H, Nagaura E, Koizumi Y (2002) Periodic intrusion of Cold Water from the Pacific Ocean into the bottom layer of the Bungo Channel in Japan. J Oceanogr 58:547–556. https://doi.org/10.1023/A:1021262609923

Kasai A, Yamada T, Takeda H (2007) Flow structure and hypoxia in Hiuchi-nada, Seto Inland Sea, Japan. Estuar Coast Shelf Sci 71:210–217. https://doi.org/10.1016/j.ecss.2006.08.001

Kim YH, Kim YB, Kim K, Kl C, Lyu SJ, Cho YK, Teague WJ (2006) Seasonal variation of the Korea Strait Bottom Cold Water and its relation to the bottom current. Geophys Res Lett 33:1–5. https://doi.org/10.1029/2006GL027625

Kobayashi S, Simpson JH, Fujiwara T, Horsburgh KJ (2006) Tidal stirring and its impact on water column stability and property distributions in a semi-enclosed shelf sea (Seto Inland Sea, Japan). Cont Shelf Res 26:1295–1306. https://doi.org/10.1016/j.csr.2006.04.006

Mellor GL, Yamada T (1982) Development of a turbulence closure model for geophysical fluid problems. Rev Geophys 20:851–875. https://doi.org/10.1029/RG020i004p00851

Nishikawa T, Hori Y, Nagai S, Miyahara K, Nakamura Y, Harada K, Tada K, Imai I (2011) Long time-series observations in population dynamics of the harmful diatom *Eucampia zodiacus* and environmental factors in Harima-Nada, eastern Seto Inland Sea, Japan during 1974–2008. Plankton Benthos Res 6:26–34. https://doi.org/10.3800/pbr.6.26

Ochi T, Takeoka H (1986) The anoxic water mass in Hiuchi Nada Part I. Distribution of the anoxic water mass. J Oceanogr Soc Jpn 42:1–11

Smagorinsky JS (1963) General circulation experiments with the primitive equations. I. The basic experiment. Mon Weather Rev 91:99–164. https://doi.org/10.1175/1520-0493(1963)091%3c0099:GCEWTP%3e2.3.CO;2

Takeoka H (2002) Progress in Seto Inland Sea research. J Oceangr 58:93–107

Takeoka H, Ochi T, Takatani K (1986) The anoxic water mass in Hiuchi-Nada Part 2. The heat and oxygen budget model. J Oceanogr Soc Jpn 42:12–21. https://doi.org/10.1007/BF02109188

Takeoka H, Koizumi Y, Kaneda A (2000) Year-to-year variation of a kyucho and a bottom intrusion in the Bungo Channel, Japan. In: Yanagi T (ed) Interactions between estuaries, coastal seas and shelf seas. Terra Scientific Publishing Company, Tokyo, pp 197–215

Wang H, Guo X, Liu Z (2019) The age of Yodo River water in the Seto Inland Sea. J Mar Syst 191:24–37. https://doi.org/10.1016/j.jmarsys.2018.12.001

Xia C, Qiao F, Yang Y, Ma J, Yuan Y (2006) Three-dimensional structure of the summertime circulation in the Yellow Sea from a wave-tide-circulation coupled model. J Geophys Res 111:1–19. https://doi.org/10.1029/2005JC003218

Yamamoto T (2003) The Seto Inland Sea-eutrophic or oligotrophic? Mar Pollut Bull 47:37–42. https://doi.org/10.1016/S0025-326X(02)00416-2

Yanagi T (2003) Coastal oceanography. TERRAPUB, Tokyo; KAP, Dordrecht

Yanagi T (2008) Outline of the Seto Inland Sea. In: Imai I, Tada K, Yanagi T, Toda T (eds) Environmental conservation of the Seto Inland Sea. International EMECS Center, Kobe, pp 2–18

Yanagi T, Higuchi H (1981) Tide and tidal current in the Seto Inland Sea. In: Proc. 28th Conf. Coast. Eng., JSCE, pp 555–558 **(in Japanese)**

Yoshie N, Guo X, Fujii N, Komorita T (2011) Ecosystem and nutrient dynamics in the Seto Inland Sea, Japan. In: Omori K, Guo X, Yoshie N, Fujii N, Handoh IC, Isobe A, Tanabe S (eds) Interdisciplinary studies on environmental chemistry—marine environmental modeling and analysis. TERRAPUB, Tokyo, pp 39–49

Yu X, Guo X (2018) Intensification of water temperature increase inside the bottom cold water by horizontal heat transport. Cont Shelf Res 165:26–36. https://doi.org/10.1016/j.csr.2018.06.006

Yu X, Guo X, Takeoka H (2016) Fortnightly variation in the bottom thermal front and associated circulation in a semienclosed

sea. J Phys Oceanogr 46:159–177. https://doi.org/10.1175/JPO-D-15-0071.1

Yuan D, Li Y, Qiao F, Zhao W (2013) Temperature inversion in the Huanghai Sea bottom cold water in summer. Acta Oceanol Sin 32:42–47. https://doi.org/10.1007/s13131-013-0287-3

Zhu J, Shi J, Guo X, Gao H, Yao X (2018) Air–sea heat flux control on the Yellow Sea Cold Water Mass intensity and implications for its prediction. Cont Shelf Res 152:14–26. https://doi.org/10.1016/j.csr.2017.10.006

Zhu J, Guo X, Shi J, Gao H (2019) Dilution characteristics of riverine input contaminants in the Seto Inland Sea. Mar Pollut Bull 141:91–103. https://doi.org/10.1016/j.marpolbul.2019.02.029

Zhu J, Shi J, Guo X (2022) Interannual variation of a bottom cold water mass in the Seto Inland Sea, Japan. Ocean Sci 18:659–673. https://doi.org/10.5194/os-18-659-2022